Catalysis Science & Technology

Accepted Manuscript

ROYAL SOCIETY OF CHEMISTRY

www.rsc.org/catalysis

Synthesis, characterization and enhanced visible light photocatalytic activity of Bi_2MoO_6/Zn-Al layered double hydroxide hierarchical heterostructures

Haiping Li[a], Quanhua Deng[b], Jingyi Liu[c], Wanguo Hou[b]*, Na Du[b], Renjie Zhang[b], Xutang Tao[a]

[a]*State Key Laboratory of Crystal Materials, Shandong University, Jinan 250100, P.R. China;*

[b]*Key Laboratory of Colloid and Interface Chemistry (Ministry of Education), Shandong University, Jinan 250100, P.R. China;*

[c]*Environment Research Institute, Shandong University, Jinan 250100, P. R. China*

* To whom correspondence should be addressed

Email: wghou@sdu.edu.cn

Telephone: +86-0531-88365460

Fax: +86-0531-88364750

Running title: Bi_2MoO_6/Zn-Al LDH heterostructures

Abstract

Bi_2MoO_6/Zn-Al layered double hydroxide (LDH) hierarchical heterostructures assembled from Bi_2MoO_6 hierarchical hollow spheres and Zn-Al LDH nanosheets were synthesized by a low-temperature hydrothermal method. X-ray diffraction, Fourier transform-infrared spectroscopy, thermogravimetric analysis and X-ray photoelectron spectroscopy (XPS) confirmed the formation of the Bi_2MoO_6/Zn-Al LDH composite. Morphologies were characterized by scanning electron microscopy and transmission electron microscopy (TEM). XPS and high resolution TEM indicated the formation of a Bi_2MoO_6/Zn-Al LDH heterojunction. Increasing the LDH content from 0 to 27.0 wt.% caused the Brunauer-Emmett-Teller (BET) specific surface area of the composite to gradually increase. The photocatalytic degradation activity for Rhodamine B (RhB) under visible light irradiation exhibited a large enhancement, followed by a decrease, with increasing LDH content. The Bi_2MoO_6/Zn-Al LDH heterostructure composite with LDH content of 5.5 wt.% showed the highest photocatalytic activity and degraded 99% of RhB in 80 min, while Bi_2MoO_6 degraded less than 50%. The average photocatalytic efficiency is enhanced by more than one time. The enhanced photocatalytic activity of the Bi_2MoO_6/Zn-Al LDH heterostructure photocatalyst was mainly attributed to the efficient separation of photoinduced electrons and holes. Superoxide radicals and holes were the major active species. The Bi_2MoO_6/Zn-Al LDH heterostructure photocatalyst exhibited excellent stability and reusability. Detailed mechanism for the enhanced photocatalytic activity was discussed in this study. This work provides an effective way to fabricate a series of Bi-based and LDH-containing heterostructure photocatalysts.

Keywords: Bi_2MoO_6, layered double hydroxide, heterostructure, photocatalysis

1. Introduction

Metal oxide semiconductors are promising photocatalysts in environmental treatment and energy conversion applications, including in the oxidation of pollutants, splitting of water, reduction of carbon dioxide, dye-sensitized solar cells, and anti-microbial and anti-fog coatings for windows and lenses [1-4]. TiO_2 is an attractive photocatalyst for wastewater treatment and other cleaning processes, because it is widely available and non-toxic [5]. However, its large band gap (3.2 eV) means it only absorbs ultraviolet light which accounts for about 4% of the solar energy. This leads to a low photocatalytic activity under sunlight conditions [5]. Visible light comprises more than 40% of the solar energy [6], so developing efficient visible light photocatalysts is a priority.

Numerous visible light active photocatalysts have been reported over the years, including Bi-based [2], Ag-based [7], In-based [8], Cu-containing [9] and Co-containing [10] photocatalysts. Bi-based semiconductors have attracted much attention, because of the widespread availability and low cost of their component materials. Reported Bi-containing compounds include Bi_2MoO_6 [2], Bi_2WO_6 [11], Bi_2S_3 [12], $Bi_2O_2CO_3$ [13], Bi_2O_3 [14], BiOCl(Br) [15], $BiVO_4$ [16], etc. Bi_2MoO_6 is a layered Aurivillius-related oxide, consisting of $[Bi_2O_2]^{2+}$layers sandwiched between MoO_4^{2-} slabs. It is a semiconductor with a smaller band gap (2.5–2.8 eV), capable of capturing visible light ($420 \leq \lambda \leq 500$ nm) and exhibiting photocatalytic activity for water splitting and the degradation of organic pollutants [17, 18]. However, the photocatalytic efficiency of Bi_2MoO_6 is not sufficient for practical application because of its low quantum yield. This is caused by the rapid recombination of photoinduced electrons and holes [19].

Coupling semiconductors with matching energetic levels of conduction band (CB) and valence band (VB) is frequently used to overcome the intrinsic limitations

of single metal oxides [2, 12, 20]. Using coupled or heterojunction photocatalysts can allow the separation rate of photoinduced charge carriers in photocatalysts to be significantly increased, resulting in higher photocatalytic activity. The Bi_2MoO_6-based heterostructure has received much attention because of its excellent visible light harvesting ability [2, 19, 21-23]. Xu et al. found that the degradation rate of Rhodamine B (RhB) by the $Bi_2O_2CO_3/Bi_2MoO_6$ heterostructure was more than 64 times faster than that of Bi_2MoO_6 under visible light irradiation [2]. They also reported that Ag_3PO_4/Bi_2MoO_6 nanocomposites possessed a much higher degradation rate for RhB and methylene blue than pure Ag_3PO_4 nanoparticles and Bi_2MoO_6 under visible light irradiation, and the 50 mol% Ag_3PO_4-loaded Bi_2MoO_6 spheres exhibited the highest photocatalytic activity [19]. The $Bi_{3.64}Mo_{0.36}O_{6.55}/Bi_2MoO_6$ heterostructure also exhibited enhanced photocatalytic activity compared with that of Bi_2MoO_6 or $Bi_{3.64}Mo_{0.36}O_{6.55}$ in the photocatalytic degradation of RhB and phenol under visible light irradiation [21]. Besides, Bi_2MoO_6/TiO_2 [23], Bi_2MoO_6/carbon nanofibers [24], Bi_2MoO_6/C_{60} [22], Bi_2O_3/Bi_2MoO_6 [25] composites and $Bi_2Mo_xW_{1-x}O_6$ solid solutions [26] all show enhanced photocatalytic activity in comparison with Bi_2MoO_6.

Herein, we report the preparation of Bi_2MoO_6/Zn-Al layered double hydroxide (LDH) composites (Scheme 1). They exhibit increased photocatalytic activity compared with Bi_2MoO_6. LDHs are layered material of the formula $[M_{1-x}^{2+}M_x^{3+}(OH)_2]^{x+}A^{n-}_{x/n}\cdot mH_2O$, where M^{2+} and M^{3+} are metal ions; x is the molar ratio of $M^{3+}/(M^{2+} + M^{3+})$; A^{n-} is a charge compensating or gallery anion; and m is the number of moles of co-intercalated water per formula weight [27]. LDH has been widely incorporated in photocatalysts [4], catalyst carriers [28] and precursors for the preparation of mixed metal oxide photocatalysts [29]. In this study, the photocatalytic activity of Bi_2MoO_6/Zn-Al LDH heterostructure composites is investigated using the model

pollutant RhB. The composite structure is characterized and the mechanism of enhanced photocatalytic activity is investigated. This study provides a new photocatalyst for the degradation of organic pollutants. It demonstrates that the formation of heterostructures containing LDH [30] can indeed greatly enhance photocatalytic performance. More importantly, this method could be further extended to synthesize a series of highly efficient visible light active Bi-based LDH-containing heterojunction photocatalysts.

2. Experimental

2.1. Materials

Sodium hydroxide (NaOH), urea, sodium carbonate (Na_2CO_3), zinc nitrate ($Zn(NO_3)_2{\cdot}6H_2O$), aluminum nitrate ($Al(NO_3)_3{\cdot}9H_2O$), ethylene glycol, ethanol, sodium molybdate ($Na_2MoO_4{\cdot}2H_2O$) and bismuth nitrate ($Bi(NO_3)_3{\cdot}5H_2O$) were purchased from Aladdin (China) and P25 TiO_2 was purchased from Degussa. All the chemicals were used without further purification. Water was obtained from a Hitech-Kflow water purification system (Hitech, China).

2.1. Synthesis of Bi_2MoO_6 hierarchical hollow spheres

Bi_2MoO_6 hierarchical hollow spheres were synthesized according to the literature [17]. Firstly, 3.373 g $Bi(NO_3)_3{\cdot}5H_2O$ and 0.842 g $Na_2MoO_4{\cdot}2H_2O$ were dissolved in 10 mL of ethylene glycol, respectively. After the two solutions were mixed together, 40 mL ethanol was slowly added into the solution, followed by stirring for 10 min. The resulting clear solution was transferred into a 100 mL teflon-lined stainless steel autoclave, followed by heated at 160 ºC for 12 h. Subsequently, the autoclaves were cooled to room temperature naturally. The products were obtained after filtered, washed with water and ethanol, and dried at 80 ºC in air. The as-prepared sample was then annealed at 400 ºC for 3 h and ground into fine

powders.

2.2. Synthesis of Bi_2MoO_6/Zn-Al LDH heterostructures

Bi_2MoO_6/Zn-Al LDH composites were prepared by coprecipitation. In brief, 0.7440 g of $Zn(NO_3)_2 \cdot 6H_2O$ and 0.4692 g of $Al(NO_3)_3 \cdot 9H_2O$ were dissolved in 30 ml of H_2O, followed by the addition of 6.0, 3.2, 1.0, or 0.5 g of Bi_2MoO_6 powder and sonification for 20 min. The dispersion pH was adjusted to 9.0 by the dropwise addition of the alkali solution containing 0.5 M NaOH and 0.4 M Na_2CO_3. After heating at 60 °C for 24 h, the products were collected by filtration, washed three times with water and dried at 60 °C in an oven. Zn-Al LDH was also prepared via a similar process, but without the addition of Bi_2MoO_6. This synthesis process is shown in Scheme 1. Prepared composites are symbolized as M1, M2, M3 and M4 with the decrease of added Bi_2MoO_6 amount, for simplicity. N doped TiO_2 (N-TiO_2) and mechanically mixed Bi_2MoO_6/Zn-Al LDH composite with LDH content of 5.5% were also prepared for photocatalytic activity comparison (see supplementary data).

2.3. Characterization

Powder X-ray diffraction (XRD) was carried out using a D/max-rA model diffractometer, with Cu Kα radiation (λ = 1.54184 Å, 40 kV, 40 mA). Fourier transform infrared (FT-IR) spectra were recorded on a Bruker Tensor27 spectrophotometer. UV-vis diffuse reflectance spectra were obtained on a Cary 100 spectrophotometer, with a $BaSO_4$ reference. Thermogravimetric (TG) analysis was carried out on a SHI-MADZU TGA-50 thermal analyzer, by heating from 30 to 800 °C, at a rate of 10 °C/min in air. X-ray photoelectron spectroscopy (XPS) was performed on a Phi 5300 esca system with Mg (Kα) radiation (photoelectron energy 1253.6 eV). The C 1s peak at 284.6 eV was used to calibrate peak positions. The composite structure was probed with transmission electron microscopy (TEM) and

high-resolution TEM (HRTEM), using a Jeol JEM-2100F microscope. Morphologies were examined with a Jeol JSM-6700F field emission-scanning electron microscopy (FE-SEM). The spatial elemental distribution of composites was investigated by energy dispersive spectrometry (EDS)-elemental mapping analysis, using an energy dispersive X-ray spectrometer equipped in the FE-SEM instrument. Inductively coupled plasma atomic emission spectroscopy (ICP-AES, IRIS Intrepid II XSP) measurement was performed to determine the contents of Zn and Al in the as-prepared samples. Photoluminescence (PL) spectra were measured using a HITACHI F-7000 spectrophotometer with the excitation wavelength of 420 nm. Specific surface areas and pore structures were probed by measuring volumetric N_2 adsorption-desorption isotherms at liquid nitrogen temperature, using an Autosorb IQ-MP instrument. Samples were degassed at 120 °C for 3 h under vacuum before measurement.

2.4. Photocatalytic activity

Photocatalytic performances of as-prepared catalysts under visible light irradiation were evaluated by the degradation of RhB at room temperature on a XPA-7 photocatalytic reaction equipment (Xujiang Electromechanical Plant, China), as shown in Fig. S1. A 400 W metal halide lamp was used as the light source, and was equipped with an ultraviolet cutoff filter ($\lambda \geqslant 420$ nm) to provide visible light. The distance between the lamp and reaction tubes containing RhB solution is about 10 cm. A water filter around the lamp is used to adsorb the infrared light. The reaction tubes around the lamp are all soaked in a constant temperature bath. For each run, 0.05 g of photocatalyst was added to 50 mL of RhB solution (10 mg/L). Prior to irradiation, the suspension was stirred in the dark for 2 h, to ensure sorption equilibrium. During irradiation, ~4 mL aliquots were collected every 20 min. These were centrifuged

(7100 ×*g*) for 10 min and analyzed by a SP-1105 visible spectrophotometer at the wavelength of 554 nm. The ratio of RhB concentration to initial concentration (C/C_0) was obtained by calculating the ratio of the corresponding absorbances. The content of total organic carbon (TOC) for the samples was measured by a TOC-5000A TOC analyzer. To evaluate the stability of the Bi_2MoO_6/Zn-Al LDH composites, recycling reactions were carried out for the photodegradation of RhB over composite M2 under visible light irradiation. After reaction, the photocatalyst was collected by centrifugation, washed, dried, and then used for the next run.

3. Results and discussion

3.1. Powder XRD, FT-IR and TG results

Fig. 1a shows powder XRD patterns of Bi_2MoO_6, Zn-Al LDH and their composites. The peaks of Bi_2MoO_6 at 10.9, 28.3, 32.6, 33.1, 36.1, 46.7, 47.2, 55.4, 55.6 and 58.5° correspond to the (020), (131), (002), (060), (151), (202), (062), (331), (133) and (262) planes, respectively, and are indexed as pure orthorhombic Bi_2MoO_6 (JCPDS file 21-0102) [2, 17]. Peaks of Zn-Al-CO_3^{2-} LDH at 11.8, 23.6, 34.0, 34.7, 37.4, 39.4, 44.2, 47.0, 48.3, 53.2, 56.6, 60.4, 61.8, 64.0 and 65.8° agree well with the (003), (006), (101), (012), (104), (015), (107), (018), (0012), (1010), (0111), (110), (113), (1013) and (116) planes, respectively (JCPDS file 48-1024), and are indexed to a hexagonal lattice with *R*3*m* rhombohedral symmetry [31]. Bi_2MoO_6/Zn-Al LDH composites contain much Bi_2MoO_6 and far less LDH, so their characteristic diffraction peaks mainly correspond to those of Bi_2MoO_6. Only the peak of LDH at 11.8° is observed, which becomes stronger with increasing LDH content (shown by the dashed line). The peak at 23.6° is also enhanced with increasing LDH content. Thus, Bi_2MoO_6 and LDH are both present within the composites.

The FT-IR spectra in Fig. 1b further indicate the existence of LDH within the

199 composites. Spectra at 1800–2500 cm^{-1} are not shown, because no absorptions are
200 observed in this range (Fig. S2). Peaks of LDH at 3441 and 1620 cm^{-1}, and of
201 Bi_2MoO_6 at 3443, 1636 and 1335 cm^{-1} are attributed to O-H vibrations [32]. Peaks at
202 432, 559 and 621 cm^{-1} for LDH are attributed to metal-O bonds. An intense peak at
203 1358 cm^{-1} and a relatively weak one at 1493 cm^{-1} are assigned to the symmetric and
204 antisymmetric O-C-O stretching vibrations of CO_3^{2-} [33]. Peaks in the spectrum of
205 Bi_2MoO_6 at 930–650 cm^{-1} are attributed to Mo-O stretching vibrations, and those at
206 600–400 cm^{-1} to Bi-O stretching and deformation vibrations [34]. The dashed lines in
207 Fig. 1b show that peaks of CO_3^{2-} and metal-O bonds are observed in the spectra of all
208 samples except Bi_2MoO_6, and they weaken with decreasing LDH content. This
209 indicates the existence of LDH in the composites.

210 Further evidence is provided by the TG curves in Fig. 1c. The thermal
211 decomposition process of composites M1–M4 is similar to that of LDH. Only 1 wt.%
212 of the weight loss from evaporating adsorbed water is observed for Bi_2MoO_6. The
213 first decomposition steps for LDH (< 183.6 °C), M1 (< 149.3 °C), M2 (< 155.3 °C),
214 M3 (< 165.4 °C) and M4 (< 173.5 °C) are due to the evaporation of absorbed and
215 intercalated water, with weight losses of 13.9, 1.7, 2.0, 4.8 and 5.3 wt.%, respectively.
216 The second weight loss (< 400 °C) is due to the removal of hydroxyl groups from
217 brucite-like layers and interlayer CO_3^{2-} [35]. The layered LDH structure is then
218 gradually destroyed upon further increasing the temperature (> 400 °C).

219 *3.2. XPS analysis*

220 Detailed information about the chemical and bonding environment in the
221 Bi_2MoO_6/LDH composite M2 and Bi_2MoO_6 was ascertained using XPS. Fig. 2a
222 shows survey scan spectra of M2 and Bi_2MoO_6 at 0–1100 eV. These indicate that C, O,
223 Bi, Mo, Zn and Al exist in M2, and C, O, Bi and Mo in Bi_2MoO_6. The C 1s peak in

the spectrum of Bi_2MoO_6 may result from adventitious carbon [24]. High resolution XPS spectra of M2 and Bi_2MoO_6 in the Bi 4f region are shown in Fig. 2b. Peaks around 158.8 and 164.1 eV for Bi_2MoO_6 are attributed to Bi $4f_{7/2}$ and Bi $4f_{5/2}$ of Bi^{3+} [19]. The corresponding peak binding energies for M2 are around 158.9 and 164.2 eV. Fig. 2c shows that the binding energies for Mo $3d_{5/2}$ and Mo $3d_{3/2}$ of Mo^{6+} in Bi_2MoO_6 are around 232.0 and 235.2 eV, respectively [24], while those for M2 are around 232.1 and 235.2 eV, respectively. The O 1s core-level spectra of M2 and Bi_2MoO_6 are shown in Fig. 2d. Peaks at 529.8 and 530.8 eV for Bi_2MoO_6 correspond to Bi-O and M-O, respectively, and those at 529.9 and 531.0 eV for M2 correspond to lattice O bound to metal cations (Zn, Al, Mo and Bi) and O bonded to the carbon species (C-O), respectively [19, 24, 30, 36]. Peaks at 531.9 eV for M2 and 531.8 eV for Bi_2MoO_6 are attributed to weakly bonded surface O, including adsorbed O species and hydroxyl groups [30]. For M2 in Fig. 2(e, f), peaks around 1022.2 and 1045.3 eV could be due to Zn 2p of Zn^{2+} [36, 37] and that at 74.2 eV corresponds to Al 2p of Al-OH [37]. Fig. 2(b, c) shows that the binding energies of Bi 4f and Mo 3d for M2 are 0.1 and 0.15 eV higher, respectively, than those of Bi_2MoO_6. Binding energy shifts of elements are associated with their chemical environment, and an increased binding energy results from a reduced electron density [37, 38]. The higher peak binding energies for Bi 4f and Mo 3d of M2 are probably caused by electron transfer from surface Bi_2MoO_6 groups to Zn-Al LDH, via the formed Zn(Al)-O-Bi(Mo) bonds. This has been reported in SnS_2/TiO_2 and Zn-Al LDH/CNTs heterostructures [37, 38]. The molar ratios of Bi/Mo/O for Bi_2MoO_6 and Zn/Al for LDH are determined to be 2.2/1/6.5 and 1.97/1, respectively, which is in the proximity of their theoretical compositions. The Zn-Al LDH formula is determined to be $[Zn_{0.66}Al_{0.34}(OH)_2](CO_3)_{0.17}{\cdot}0.87H_2O$, where the water number per formula weight is calculated from the TG result. These results

indicate the formation of a Bi_2MoO_6/Zn-Al LDH composite. Contents of Zn and Al in the as-prepared samples measured by the ICP-AES method are listed in Table S1. The calculated Zn/Al ratio (1.99 $\pm$ 0.02) and LDH formula are in accordance with the XPS result. All the samples exhibit the similar LDH formula. The LDH (without crystal water) contents of composites M1□M4 are determined to be 5.4%, 10.1%, 24.5% and 41.9%, respectively. These are very close to the theoretical values obtained from initial reactant amounts. The Zn/Bi molar ratio of M2 is calculated to be 0.2, which is much lower than that (1.5) obtained from the XPS result, indicating that Zn-Al LDH nanosheets are mainly dispersed on the surface of the Bi_2MoO_6 spheres.

3.3. Morphology

Morphologies were observed by FESEM, TEM and HRTEM. Figs. 3a and 4a indicate that hierarchically structured Bi_2MoO_6 hollow spheres are present, with diameters of 1–2 μm [17]. The as-prepared Bi_2MoO_6 spheres are similar to those previously reported [17]. Figs. 3d and 4b show that the spheres in the Bi_2MoO_6/Zn-Al LDH composite M2 are well retained, but their hollow structure is difficult to observe. This is probably due to the formed LDH blocking the sphere holes. Hexagonal Zn-Al LDH nanosheets [39] of size 100–200 nm are clearly observed adhering to the surface of the Bi_2MoO_6 spheres in Figs. 3(b, c) and 4c. EDS and elemental mapping analyses indicate that Zn, Al, Mo and Bi are homogeneously distributed throughout the surface of composite M2 as shown in Fig. 3e. This indicates a homogeneous distribution of LDH on the Bi_2MoO_6 sphere surfaces. HRTEM images in Fig. 4(d, e) show the anchoring of LDH nanosheets on the Bi_2MoO_6 spheres, and two distinct lattice fringes are observed in Fig. 4f. One set of fringes are spaced by ~0.192 nm, corresponding to the (018) plane of Zn-Al LDH. Another set are spaced by ~0.166 nm, corresponding to the (331) lattice spacing of the orthorhombic phase of Bi_2MoO_6. The XPS and

HRTEM analyses confirm that the Bi_2MoO_6/Zn-Al LDH heterojunction was formed.

3.4. N_2 sorption isotherms

Fig. 5 shows N_2 adsorption-desorption isotherms of Zn-Al LDH, Bi_2MoO_6 and their composites. All isotherms are of type IV, which is usually associated with capillary condensation in mesopores [29]. The type H3 hysteresis loops at high P/P_0 reflect the formation of slit-shaped pores from aggregates of flaky LDH and/or Bi_2MoO_6 [40]. According to the BET equation fitting results, the specific surface areas of LDH, Bi_2MoO_6, and their composites M1, M2, M3 and M4 are 78.6, 7.7, 14.1, 29.6, 32.7 and 36.3 m^2/g, respectively. This indicates that the gradual increase in composite BET specific surface area with LDH content maybe results from the large specific surface area of LDH itself.

Pore size distributions were calculated by the Barrett-Joyner-Halenda (BJH) method. As is shown in the right panel of Fig. 5, bimodal pore size distributions are observed for all samples. Pore diameters of LDH are ~3.1 and 17.4 nm, while those of Bi_2MoO_6 and the composites M1–M4 are ~2.2 and 17–31 nm, respectively, all of which are characteristic of mesopores. The occurrence of bimodal pore-size distributions is attributed to the existence of hierarchical structures [41].

3.5. Photocatalytic activity

The visible light photocatalytic activity of the as-prepared Zn-Al LDH, Bi_2MoO_6 and Bi_2MoO_6/Zn-Al LDH composites M1–M4 was evaluated in the degradation of RhB in aqueous solution. Adsorption equilibrium is reached for all photocatalysts tested, after stirring for 2 h in the dark (Fig. S3). Fig. 6a shows that when the solution was irradiated with visible light for 100 min in the absence of any catalyst, little change in RhB concentration was observed. This indicates that the photodegradation of RhB was negligible [20]. As the LDH content increases from 0 to 27.0 wt.%, the

photocatalytic activity of the Bi_2MoO_6/LDH composite is gradually enhanced, and then decreases, with composite M2 exhibiting the highest activity (Fig. 6a). The photoactivity of M2 is higher than that of Bi_2MoO_6, Zn-Al LDH, commercial P25 TiO_2 powder, N doped TiO_2 and mechanically mixed Bi_2MoO_6/LDH composite (Fig. 6b). After 80 min, about 99% of RhB is removed by composite M2 while less than 50% is removed by Bi_2MoO_6. The average photocatalytic efficiency is enhanced by more than one time. The top inset indicates the color change of the suspension containing M2 (Fig. 6a). However, the TOC result (Fig. S4) indicates only 30% of RhB is mineralized over M2 after 100 min and more irradiation time is needed to make the substrate completely mineralized. But the mineralization rate of RhB over M2 is higher than that over Bi_2MoO_6 since Bi_2MoO_6 mineralizes RhB by only 14% after 100 min. The above results show that Bi_2MoO_6/Zn-Al LDH heterojunction composites containing an appropriate amount of LDH exhibit much higher photocatalytic activity than Bi_2MoO_6 under visible light irradiation.

Fig. 7a shows that no apparent deactivation of the photocatalysts is observed after five consecutive runs and the RhB degradation efficiency declines by less than 2%. XRD patterns of composite M2 before and after the photocatalytic reactions are shown in Fig. 7b, and indicate that the M2 crystal structure remains constant through the reactions. The as-synthesized Bi_2MoO_6/Zn-Al LDH heterojunction photocatalyst exhibits excellent stability in the visible light photochemical degradation reactions.

3.6. Photocatalytic mechanism

Fig. 8 shows the UV-vis diffusive reflectance spectra of Bi_2MoO_6, LDH and their composites. Bi_2MoO_6 presents the photoabsorption property from the UV light region to visible light shorter than 490 nm. The absorbance of LDH is quite low. Samples M1–M3 exhibit similar absorbance as Bi_2MoO_6, but the sample M4 containing the

most LDH presents the lower, which may be caused by that LDH covers the active sites on the surface of Bi_2MoO_6 spheres. For crystalline semiconductors, their optical band gap could be calculated from the absorption spectra using the equation $\alpha hv = A(hv - E_g)^{n/2}$, where α, v, A, and E_g are the absorption coefficient, light frequency, proportionality constant, and optical band gap, respectively (See supplementary data). n depends upon the characteristics of transition in a semiconductor (n = 1 for a directly allowed transition and n = 4 for indirectly allowed transition), and n = 1 was confirmed here by Parida's method [42]. The band gaps of Bi_2MoO_6, Zn-Al LDH and composites M1–M4 are 2.72 eV, 3.07 eV, 2.71 eV, 2.72 ev, 2.71 eV, and 2.74 eV, respectively (see the inset). The band gaps of M1, M2 and M3 are proximately equal to that of Bi_2MoO_6 (2.72 eV). According to the Mulliken electronegativity theory [43], the top of VB and the bottom of CB of Bi_2MoO_6 are calculated to be +2.41 and -0.31 eV, respectively, while the VB and CB of LDH ($[Zn_{0.66}Al_{0.34}(OH)_2](CO_3)_{0.17}$) are estimated as +3.62 and +0.55 eV, respectively. Herein, "H_2O" in the formula of LDH is not included in the calculation of VB and CB potentials (see supplementary data).

The photocatalytic mechanism of Bi_2MoO_6/Zn-Al LDH composites for degrading RhB can be proposed as following:

$$Bi_2MoO_6 + hv \longrightarrow e^-(Bi_2MoO_6) + h^+(Bi_2MoO_6) \quad (1)$$

$$e^-(Bi_2MoO_6) + O_2 \longrightarrow \bullet O_2^- \quad (2)$$

$$LDH + e^-(Bi_2MoO_6) \longrightarrow e^-(LDH) \quad (3)$$

$$2e^-(LDH) + O_2 + 2H^+ \longrightarrow H_2O_2 \quad (4)$$

$$h^+(Bi_2MoO_6) + OH^- \longrightarrow \bullet OH \quad (5)$$

$$\bullet O_2^- + 2H^+ + e^-(Bi_2MoO_6) \longrightarrow H_2O_2 \quad (6)$$

$$H_2O_2 + e^-(Bi_2MoO_6) \longrightarrow \bullet OH + OH^- \quad (7)$$

$$\bullet OH + RhB \longrightarrow \text{degraded or mineralized products} \quad (8)$$

$\bullet O_2^-$ + RhB ⟶ degraded or mineralized products (9)

$h^+(Bi_2MoO_6)$ + RhB ⟶ degraded or mineralized products (10)

Photogenerated electrons from Bi_2MoO_6 reduce surface chemisorbed O_2 to give superoxide radicals ($\bullet O_2^-$) ($E(O_2/\bullet O_2^-)$ = -0.046 eV *vs.* NHE) (Equation 1□2). Photogenerated holes (h^+) oxidize OH^- to give •OH ($E(OH^-/\bullet OH)$ = +1.99 eV *vs.* NHE) [44] (Equation 5), and •OH can also be generated from $\bullet O_2^-$ (Equation 6□7)[45]. All of h^+, e^-, $\bullet O_2^-$ and •OH are possible active species for the photodegradation of organic pollutants [14, 42, 45]. To evaluate the role of these active species, individual scavengers were added to the photodegradation system. Scavengers used were tert-butyl alcohol (*t*-BuOH) for •OH [42], sodium oxalate for h^+ [14], $K_2Cr_2O_7$ for e^- [45] and benzoquinone (BQ) for $\bullet O_2^-$ [42]. Fig. 9 shows that the addition of *t*-BuOH causes no appreciable change in the photodegradation efficiency of M2. This indicates that •OH is not significant in the photocatalytic process (Equation 8). A significant suppression of photocatalytic performance is observed when BQ is added, confirming the important role of $\bullet O_2^-$ in the photodegradation process (Equation 9). The photodegradation activity of M2 declines to some extent after sodium oxalate is added, implying that h^+ plays a role (Equation 10). After $K_2Cr_2O_7$ is added, the photodegradation activity of M2 declines a little, indicating that e^- plays a minor role. Thus, the photocatalytic process is mainly governed by $\bullet O_2^-$ and h^+ (Equation 9□10), rather than •OH and e^-, which is in agreement with the $Bi_2O_2CO_3/Bi_2MoO_6$ nanocomposite [2] and heterostructured Bi_2O_3/Bi_2MoO_6 microsphere [25] systems.

The enhanced photocatalytic performance of the Bi_2MoO_6/Zn-Al LDH heterojunction photocatalyst is ascribed to the charge transfer process of the heterostructure (Equation 3), as illustrated in Scheme 2. Although Zn-Al LDH cannot be excited by visible light, it can accept photogenerated electrons transferred from

374 Bi_2MoO_6 because it has a more positive CB (+0.55 eV) than Bi_2MoO_6 (-0.31 eV).
375 Electrons located in the CB of LDH can reduce O_2 to H_2O_2 ($E(O_2/H_2O_2)$ = +0.70 eV)
376 (Equation 4). Thus, photogenerated electrons and holes are effectively separated, and
377 the possibility of electron-hole recombination decreases, which can also be deduced
378 from the photoluminescence (PL) spectra (Fig. S5). Although LDH exhibits very high
379 PL intensity, the composite M2 exhibits lower intensity than Bi_2MoO_6. This
380 demonstrates a reduced electron-hole recombination for M2. Correspondingly,
381 remaining holes can directly oxidize absorbed RhB. The increased specific surface
382 area of composites M1–M2 may be not the major reason for the enhancement of their
383 photoactivity since the specific surface area change is little and probably caused by
384 the specific surface area of increased LDH itself. Though the specific surface area of
385 M1 and M2 is higher than that of Bi_2MoO_6, the RhB adsorption amount on the former
386 is less than that on the latter (Fig. S3). The decreased adsorption amount of RhB on
387 composites M1□M4 is probably due to the electrostatic repulsion between LDH and
388 RhB both of which are charged positively. The adsorption of RhB on the surface of
389 photocatalysts usually makes for the enhancement of photocatalytic efficiency [46]. But
390 the higher photodegradation efficiency despite lower adsorption amount of RhB over
391 M2 than that over Bi_2MoO_6 indicates that the adsorptive capability of studied
392 Bi_2MoO_6/LDH composites is not the main factor influencing their photocatalytic
393 activity. The decreased activity of M3 and M4 in Fig. 6 probably results from excess
394 LDH covering active sites on the Bi_2MoO_6 surface [20] and the reduced Bi_2MoO_6
395 content.

396 **4. Conclusions**

397 Bi_2MoO_6/Zn-Al LDH hierarchical heterostructures were prepared via a
398 low-temperature hydrothermal process. XRD, FT-IR, TG, XPS, TEM, HRTEM and

SEM/elemental mapping analyses were used for characterization. The heterostructure was composed of Bi_2MoO_6 hollow spheres and LDH nanosheets, and exhibited enhanced photodegradation efficiency for RhB compared with Bi_2MoO_6 and LDH. This resulted from a reduced photogenerated electron-hole recombination, caused by the transfer of electrons from Bi_2MoO_6 to LDH. The heterojunction composite with LDH content of 5.5 wt.% exhibited the highest photocatalytic activity, and less than 2% decline in activity was observed after five photocatalysis cycles. This heterostructure photocatalyst has potential in environmental remediation and wastewater treatment. This method may provide a new route for preparing efficient Bi-based LDH-containing heterostructures for light-harvesting and energy conversion applications.

Acknowledgements

The present work is supported financially by the National Natural Science Foundation of China (No. 21173135) and the Specialized Research Fund for the Doctoral Program of Higher Education of China (No. 20110131130008).

References

1. P. Yang and J.-M. Tarascon, *Nat Mater*, 2012, **11**, 560-563.
2. Y.-S. Xu and W.-D. Zhang, *Appl Catal B*, 2013, **140-141**, 306-316.
3. W. Wang, T. W. Ng, W. K. Ho, J. Huang, S. Liang, T. An, G. Li, J. C. Yu and P. K. Wong, *Appl Catal B*, 2013, **129**, 482-490.
4. K. Teramura, S. Iguchi, Y. Mizuno, T. Shishido and T. Tanaka, *Angew Chem Int Edit*, 2012, **51**, 8008-8011.
5. L. Ye, L. Tian, T. Peng and L. Zan, *J Mater Chem*, 2011, **21**, 12479-12484.
6. G. Xi and J. Ye, *Chem Commun (Camb)*, 2010, **46**, 1893-1895.
7. H. Dong, G. Chen, J. Sun, C. Li, Y. Yu and D. Chen, *Appl Catal B*, 2013, **134-135**, 46-54.
8. L. Shang, C. Zhou, T. Bian, H. Yu, L.-Z. Wu, C.-H. Tung and T. Zhang, *J Mater Chem A*, 2013, **1**, 4552-4558.
9. W. Shi, J. Shi, S. Yu and P. Liu, *Appl Catal B*, 2013, **138-139**, 184-190.
10. Z. P. Chen, J. Xing, H. B. Jiang and H. G. Yang, *Chemistry*, 2013, **19**, 4123-4127.
11. L. Ge, C. Han and J. Liu, *Appl Catal B*, 2011, **108-109**, 100-107.
12. H. Cheng, B. Huang, X. Qin, X. Zhang and Y. Dai, *Chem Commun*, 2012, **48**, 97-99.
13. H. Gan, G. Zhang and H. Huang, *J Hazard Mater*, 2013, **250-251**, 131-137.
14. X. Xiao, R. Hu, C. Liu, C. Xing, C. Qian, X. Zuo, J. Nan and L. Wang, *Appl*

Catal B, 2013, **140-141**, 433-443.

15. H. Gnayem and Y. Sasson, *ACS Catalysis*, 2013, **3**, 186-191.
16. J. Yang, D. Wang, X. Zhou and C. Li, *Chem Eur J*, 2013, **19**, 1320-1326.
17. G. Tian, Y. Chen, W. Zhou, K. Pan, Y. Dong, C. Tian and H. Fu, *J Mater Chem*, 2011, **21**, 887-892.
18. M. Shang, W. Wang, J. Ren, S. Sun and L. Zhang, *Nanoscale*, 2011, **3**, 1474-1476.
19. Y. S. Xu and W. D. Zhang, *Dalton Trans*, 2013, **42**, 1094-1101.
20. S. Ye, L.-G. Qiu, Y.-P. Yuan, Y.-J. Zhu, J. Xia and J.-F. Zhu, *J Mater Chem A*, 2013, **1**, 3008-3015.
21. J. Ren, W. Wang, M. Shang, S. Sun and E. Gao, *ACS Appl Mater Interfaces*, 2011, **3**, 2529-2533.
22. X. Zhao, H. Liu, Y. Shen and J. Qu, *Appl Catal B*, 2011, **106**, 63-68.
23. M. Zhang, C. Shao, J. Mu, Z. Zhang, Z. Guo, P. Zhang and Y. Liu, *CrystEngComm*, 2012, **14**, 605-612.
24. M. Zhang, C. Shao, J. Mu, X. Huang, Z. Zhang, Z. Guo, P. Zhang and Y. Liu, *J Mater Chem*, 2012, **22**, 577-584.
25. Y.-S. Xu, Z.-J. Zhang and W.-D. Zhang, *Mater Res Bull*, 2013, **48**, 1420-1427.
26. L. Zhou, M. Yu, J. Yang, Y. Wang and C. Yu, *J Phys Chem C*, 2010, **114**, 18812-18818.
27. D. G. Evans and X. Duan, *Chem Commun*, 2006, 485-496.

28. Z. Huang, P. Wu, Y. Lu, X. Wang, N. Zhu and Z. Dang, *J Hazard Mater*, 2013, **246-247**, 70-78.

29. S. Cho, J.-W. Jang, K.-j. Kong, E. S. Kim, K.-H. Lee and J. S. Lee, *Adv Funct Mater*, 2013, **23**, 2348-2356.

30. R. Lu, X. Xu, J. Chang, Y. Zhu, S. Xu and F. Zhang, *Appl Catal B*, 2012, **111-112**, 389-396.

31. Y. Zhao, S. Zhang, B. Li, H. Yan, S. He, L. Tian, W. Shi, J. Ma, M. Wei, D. G. Evans and X. Duan, *Chem Eur J*, 2011, **17**, 13175-13181.

32. J. M. Fernández, C. Barriga, M. A. Ulibarri, F. M. Labajos and V. Rives, *Chem Mater*, 1997, **9**, 312-318.

33. A. A. Khassin, T. M. Yurieva, G. N. Kustova, I. S. Itenberg, M. P. Demeshkina, T. A. Krieger, L. M. Plyasova, G. K. Chermashentseva and V. N. Parmon, *J Mol Catal A*, 2001, **168**, 193-207.

34. F. Trifirò, H. Hoser and R. D. Scarle, *J Catal*, 1972, **25**, 12-24.

35. A. A. A. Ahmed, Z. A. Talib and M. Z. b. Hussein, *Appl Clay Sci*, 2012, **56**, 68-76.

36. K. Parida and L. Mohapatra, *Dalton Trans*, 2012, **41**, 1173-1178.

37. H. Wang, X. Xiang and F. Li, *AIChE J*, 2010, **56**, 768-778.

38. Z. Zhang, C. Shao, X. Li, Y. Sun, M. Zhang, J. Mu, P. Zhang, Z. Guo and Y. Liu, *Nanoscale*, 2013, **5**, 606-618.

39. Y. Zhang, Z. Chen, S. Liu and Y.-J. Xu, *Appl Catal B*, 2013, **140-141**, 598-607.

40. J. L. Gunjakar, I. Y. Kim, J. M. Lee, N. S. Lee and S. J. Hwang, *Energy Environ Sci*, 2013, **6**, 1008-1017.

41. R. Asahi, T. Morikawa, T. Ohwaki, K. Aoki and Y. Taga, *Science*, 2001, **293**, 269-271.

42. L. Mohapatra, K. Parida and M. Satpathy, *J Phys Chem C*, 2012, **116**, 13063-13070.

43. M. R. Hoffmann, S. T. Martin, W. Choi and D. W. Bahnemann, *Chem Rev*, 1995, **95**, 69-96.

44. D. Zhang, J. Li, Q. Wang and Q. Wu, *J Mater Chem A*, 2013, **1**, 8622-8629.

45. S. Ge and L. Zhang, *Environ Sci Technol*, 2011, **45**, 3027-3033.

46. R. D. Martínez-Orozco, H. C. Rosu, S. W. Lee and V. Rodríguez-González, *J Hazard Mater*, 2013, **263**, 52-60.

Figure Captions

Fig. 1. XRD patterns (a), FT-IR spectra (b) and TG curves (c) of Bi_2MoO_6, Zn-Al LDH and their composites M1–M4.

Fig. 2. XPS survey spectra (a) and high-resolution XPS spectra of the Bi 4f (b), Mo 3d (c) and O 1s (d) regions, for the Bi_2MoO_6/Zn-Al LDH composite M2 and Bi_2MoO_6. High-resolution XPS spectra of the Zn 2p (e) and Al 2p (f) regions for M2.

Fig. 3. FE-SEM images of Bi_2MoO_6 (a) and the Bi_2MoO_6/Zn-Al LDH composite M2 (b–d), and elemental mapping/FE-SEM analyses of M2 (e).

Fig. 4. TEM images of Bi_2MoO_6 (a) and the Bi_2MoO_6/Zn-Al LDH composite M2 (b and c), and HRTEM images of M2 (d–f).

Fig. 5. N_2 adsorption-desorption isotherms (left) and pore size distributions (right) of Zn-Al LDH, Bi_2MoO_6 and their composites M1–M4.

Fig. 6. Photocatalytic degradation and color change (for M2) of RhB, over various photocatalysts after different reaction time.

Fig. 7. Five consecutive RhB photodegradation cycles of the Bi_2MoO_6/Zn-Al LDH composite M2 under visible light irradiation (a); Powder XRD patterns of M2 before and after reactions (b).

Fig. 8. UV-vis diffusive reflectance spectra of Zn-Al LDH, Bi_2MoO_6 and their composites M1–M4.

Fig. 9. Photocatalytic degradation efficiency for RhB over the Bi_2MoO_6/Zn-Al LDH composite M2 with different scavengers: 20 mM *t*-BuOH, 0.2 mM sodium oxalate, 10 mM $K_2Cr_2O_7$ and 0.1 mM BQ.

Scheme 1. Schematic illustration showing the fabrication of Bi_2MoO_6/Zn-Al LDH composites.

Scheme 2. Schematic illustration showing RhB degradation over a Bi_2MoO_6/Zn-Al LDH composite under visible light irradiation.

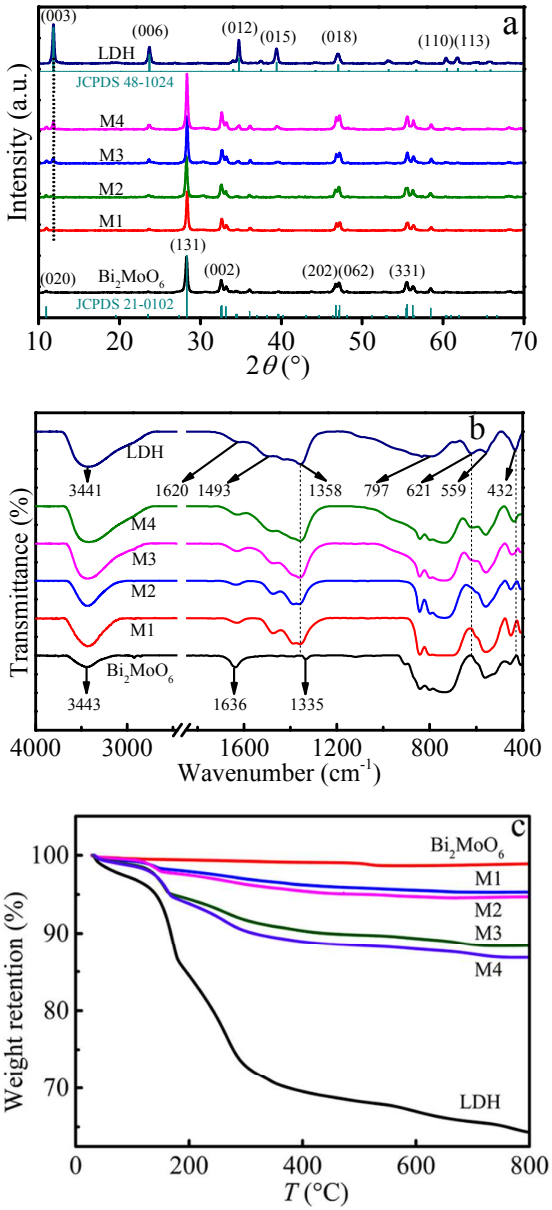

Fig. 1. XRD patterns (a), FT-IR spectra (b) and TG curves (c) of Bi_2MoO_6, Zn-Al LDH and their composites M1–M4.

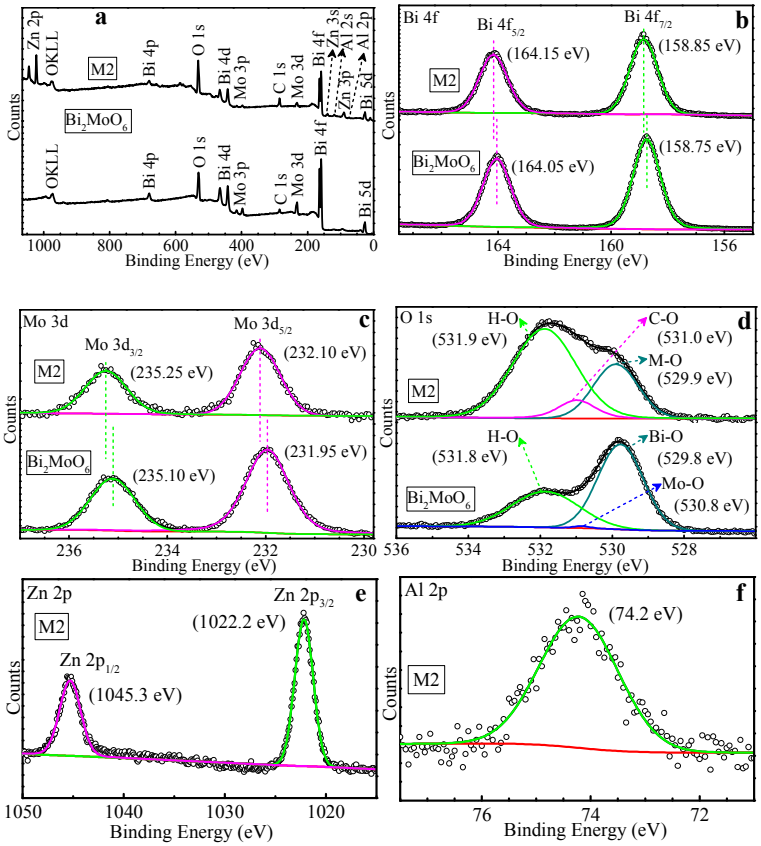

Fig. 2. XPS survey spectra (a) and high-resolution XPS spectra of the Bi 4f (b), Mo 3d (c) and O 1s (d) regions, for the Bi_2MoO_6/Zn-Al LDH composite M2 and Bi_2MoO_6. High-resolution XPS spectra of the Zn 2p (e) and Al 2p (f) regions for M2.

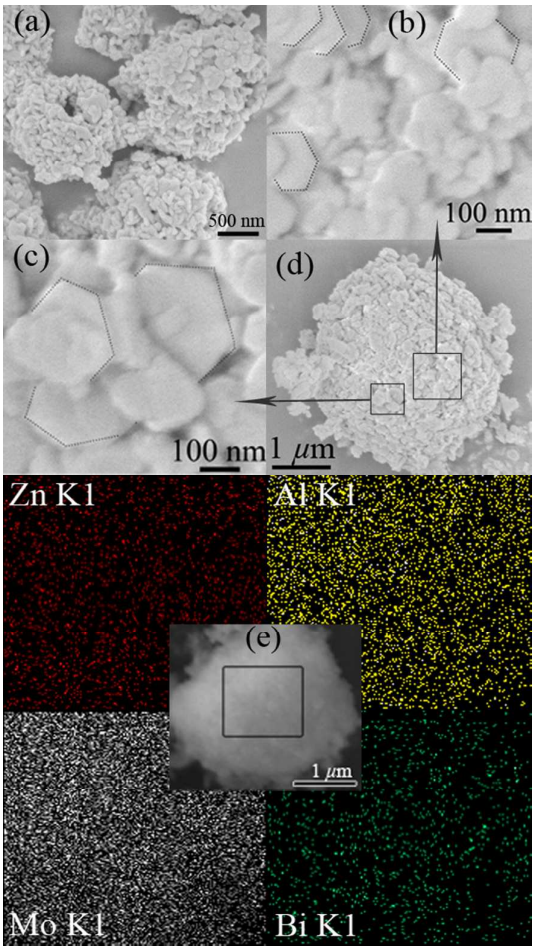

Fig. 3. FE-SEM images of Bi_2MoO_6 (a) and the Bi_2MoO_6/Zn-Al LDH composite M2 (b–d), and elemental mapping/FE-SEM analyses of M2 (e).

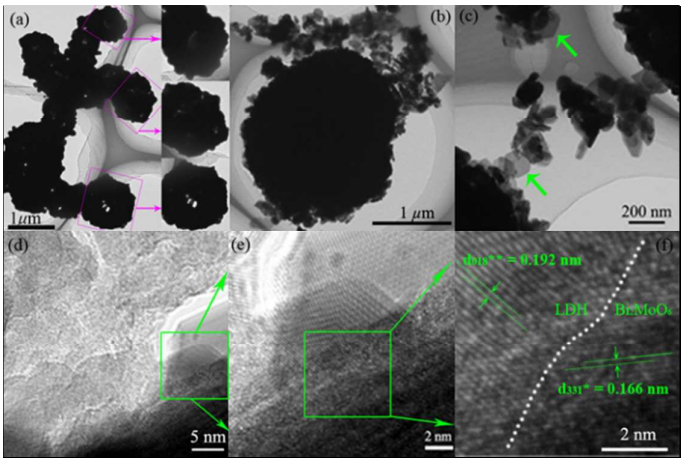

Fig. 4. TEM images of Bi_2MoO_6 (a) and the Bi_2MoO_6/Zn-Al LDH composite M2 (b and c), and HRTEM images of M2 (d–f).

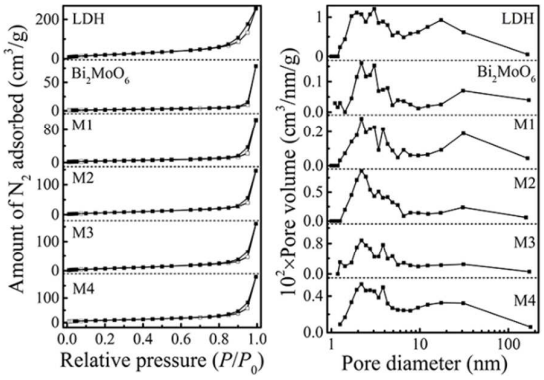

Fig. 5. N_2 adsorption-desorption isotherms (left) and pore size distributions (right) of Zn-Al LDH, Bi_2MoO_6 and their composites M1–M4.

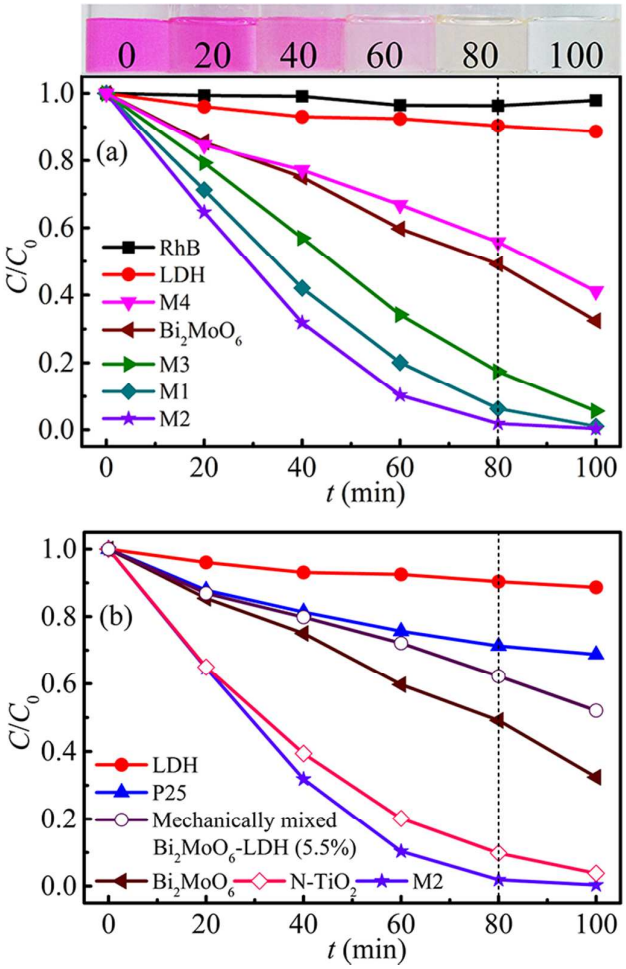

Fig. 6. Photocatalytic degradation and color change (for M2) of RhB, over various photocatalysts after different reaction time.

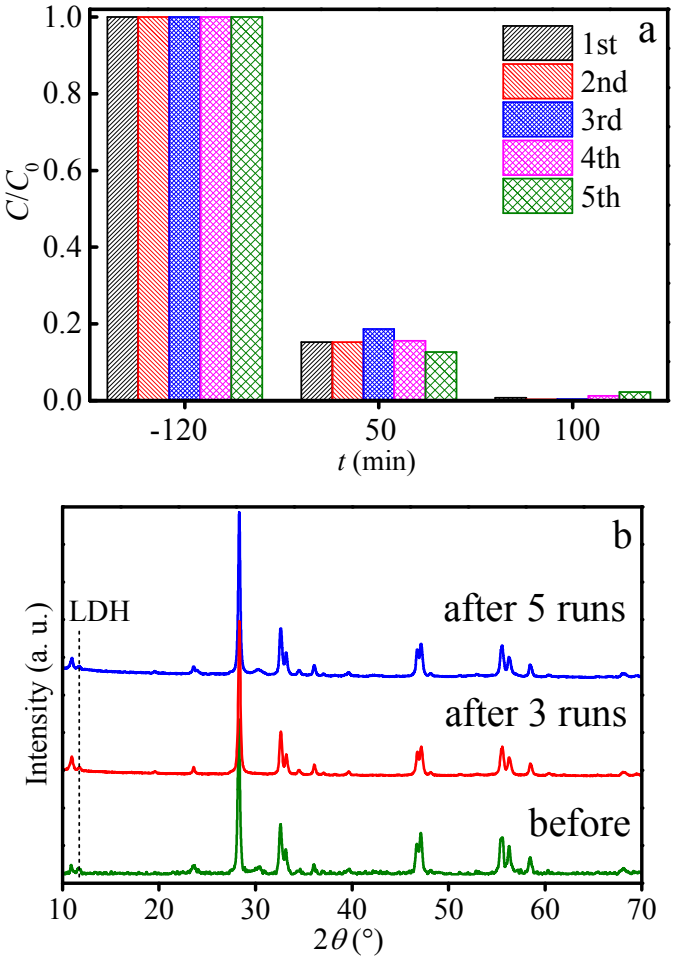

Fig. 7. Five consecutive RhB photodegradation cycles of the Bi_2MoO_6/Zn-Al LDH composite M2 under visible light irradiation (a); Powder XRD patterns of M2 before and after reactions (b).

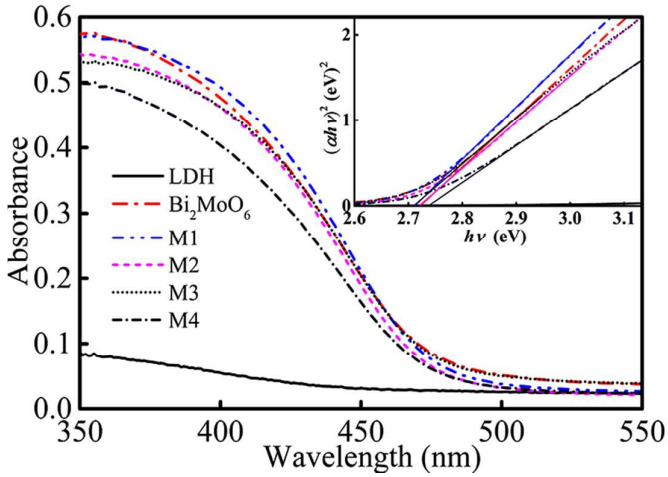

Fig. 8. UV-vis diffusive reflectance spectra of Zn-Al LDH, Bi_2MoO_6 and their composites M1–M4.

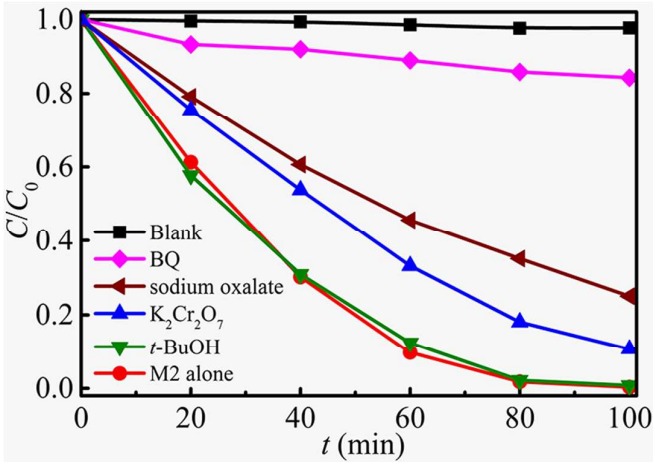

Fig. 9. Photocatalytic degradation efficiency for RhB over the Bi_2MoO_6/Zn-Al LDH composite M2 with different scavengers: 20 mM *t*-BuOH, 0.2 mM sodium oxalate, 10 mM $K_2Cr_2O_7$ and 0.1 mM BQ.

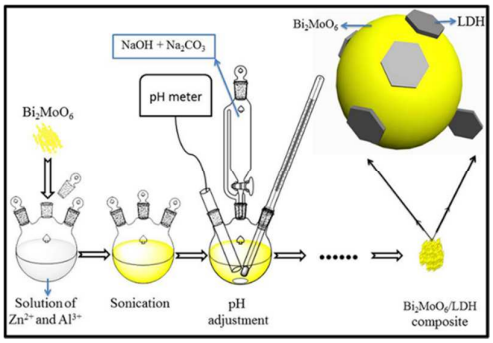

Scheme 1. Schematic illustration showing the fabrication of Bi_2MoO_6/Zn-Al LDH composites.

82

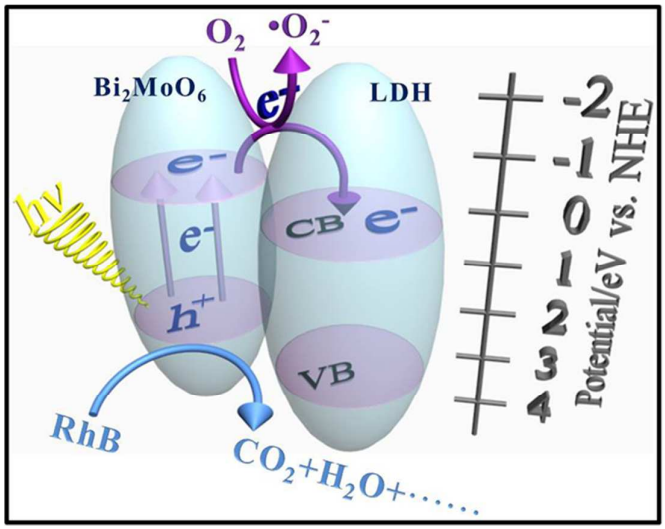

83

84 Scheme 2. Schematic illustration showing RhB degradation over a Bi_2MoO_6/Zn-Al

85 LDH composite under visible light irradiation.

86